Chapter 20
Wavefront and Coherence Characteristics of Extreme UV and Soft X-ray Sources

Bernd Schäfer, Bernhard Flöter, Tobias Mey and Klaus Mann

Abstract The first part of this chapter comprises setups and results of the determination of wavefront and beam parameters for different EUV sources (free-electron lasers, HHG-sources, synchrotron radiation) by self supporting Hartmann-Sensors. We present here i.a. a sensor applied for alignment of the ellipsodial mirror at FLASH beamline 2, yielding a reduction of the rms-wavefront aberrations by more than a factor of 3. In the second part we report on the characterization of the Free-Electron-Laser FLASH at DESY by a quantitative determination of the Wigner distribution function. The setup, comprising an ellipsodial mirror and a moveable extreme UV sensitive CCD detector, enables the mapping of two-dimensional phase space corresponding to the horizontal and vertical coordinate axes, respectively. Furthermore, an extended setup utilizing a torodial mirror for complete 4D-Wigner reconstruction has been accomplished and tested using radiation from a multimode Nd:VO4 laser.

PACS Subject Classification: 42.15.Dp · 42.25.Kb · 42.55.Vc

20.1 Introduction

Electromagnetic radiation in the extreme UV and soft X-ray spectral range is of steadily increasing importance in fundamental research and industrial applications. For instance, the molecular structure of proteins and viruses has become accessible by coherent diffractive imaging techniques; currently, lithographic processes for the microchip production are being adapted to the extreme UV wavelength of 13.5 nm. For both examples, a comprehensive beam characterization is an essential condition for an ideal use of the available photons, and only exact knowledge of the illuminating radiation field allows for further improvements of spatial resolution and

B. Schäfer (✉) · B. Flöter · T. Mey · K. Mann
Laser-Laboratorium Göttingen eV., Hans-Adolf-Krebs-Weg 1,
37077 Göttingen, Germany
e-mail: bernd.schaefer@llg-ev.de

K. Mann
e-mail: kmann@llg-ev.de

T. Salditt et al. (eds.), *Nanoscale Photonic Imaging*, Topics in Applied Physics 134,
https://doi.org/10.1007/978-3-030-34413-9_20

reliability in nanoscale imaging and structuring. To this end, pioneering developments in large-scale and table-top light sources of extreme ultraviolet (EUV) radiation are necessarily complemented by implementing advanced beam characterization techniques. The Laser-Laboratorium Göttingen has developed metrological tools and analysis procedures for proper characterization of the propagation behaviour of short wavelength radiation. This contribution addresses wavefront measurements on free electron lasers (FELs) and high harmonic (HHG) sources emitting in the extreme UV and soft X-ray range. The diagnostics schemes based on Hartmann sensing accomplish, on the one hand, comprehensive beam analysis including prediction of focal distributions, on the other also fine-adjustment of beamline optics for optimization of peak intensities. Additionally, the coherence of laser beams is analyzed by measurements of the Wigner distribution function. This method is applied to the photon beam of the free-electron laser FLASH, resulting in the entire characterization of its propagation properties, including both global and local degrees of spatial coherence.

20.2 Wavefront Metrology and Beam Characterization with Hartmann Sensors

20.2.1 Hartmann Wavefront Sensing

The wavefront or phase distribution of a radiation field carries quantitative information over its directional distribution, and is therefore of utmost importance for the design of beam transport optics. On-line recording of the wavefront can also accomplish an optimization of the beam focusability by precision alignment of optical elements. Other relevant areas are the monitoring and possible reduction of thermal lensing effects, on-line resonator adjustment, or "at wavelength" testing of optics including Zernike analysis. The wavefront of a radiation source is defined as the surface $w(x, y)$ that is normal to the local direction of energy propagation in the electromagnetic field [1], i.e. normal to the Poynting vector (x, y) at the measurement plane (cf. Fig. 20.1, left). In case of highly coherent radiation, $w(x, y)$ is a surface of constant phase. The phase distribution $\Phi(x, y)$ is then related to the wavefront according to

$$\Phi(x, y) = \frac{2\pi}{\lambda} \cdot w(x, y), \tag{20.1}$$

where λ is the mean wavelength of the light.

A variety of different techniques has been developed for wavefront sensing. Interferometric devices, as there are Twyman-Green, common path, lateral shear, Mach-Zehnder or Sagnac interferometers, can be applied over the full wavelength spectrum for which detectors and optical materials are available, provided that the coherence is sufficient for detectable levels of interference. Alternatively, phase gradient measurement techniques, in particular Hartmann or Hartmann-Shack, can be used with both

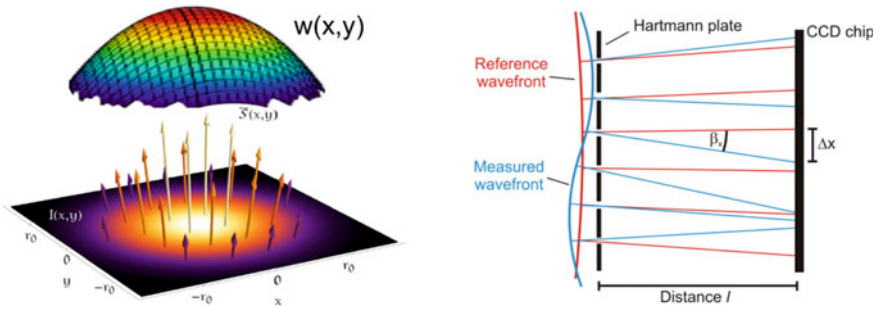

Fig. 20.1 left: Definition of the wavefront of a radiation field; right: Measurement principle of Hartmann-type wavefront sensors (cf. text)

coherent and incoherent beams. In these instruments, the gradients of either wavefront or phase are measured, from which the two-dimensional phase distribution can be reconstructed. The Hartmann principle [1] is based on a subdivision of a beam into a number of beamlets (see Fig. 20.1, right). This is either accomplished by an opaque screen with pinholes placed on a regular grid (Hartmann sensor), or by a lenslet or micro-lens array (Hartmann-Shack sensor). The latter accomplishes a better radiation collection efficiency and a wider dynamic range. For this reason, Hartmann-Shack sensors are already widely used for Vis, NIR and UV radiation. However, since no transmissive optical materials for the fabrication of micro-lens arrays are available at extreme UV and soft X-ray wavelengths, only the Hartmann appoach using pinhole arrays is appropriate in this spectral region. The spot distribution produced by the segmenting array is recorded at a distance l by a position sensitive detector, most commonly a CCD camera. The position of the beamlet centroids is determined within each sub-aperture, both for the beam under test and a reference wavefront. The latter is provided preferably by a well collimated laser beam (plane wave), or a well defined spherical wave, using e.g. the output of a monomode fiber or the Airy pattern produced behind a diffracting pin-hole. The displacement of the spot centroid Δx divided by the distance l yields the local wavefront gradient β_x inside one subaperture relative to the reference wavefront (see Fig. 20.1, right). By direct integration or modal fitting techniques using Zernike or Legendre polynomials, the wavefront $w(x, y)$ is reconstructed from these local gradients [2, 3] and afterwards corrected for tip/tilt and defocus [1]. A detailed description of the wavefront reconstruction methods is given in the references. The main advantages of the Hartmann technique compared to interferometric devices are

- suitability for fully and partially coherent beams,
- no requirement of spectral purity,
- no ambiguity with respect to 2π increment in phase angle,
- compact and robust design.

Hartmann-Shack and Hartmann wavefront sensors can be successfully applied for real-time laser beam characterization, since they are recording simultaneously (i.e. in

single pulses) the wavefront (directional distribution) $w(x, y)$ and the beam profile or intensity distribution $I(x, y)$ of a radiation field [4, 5]. The latter is obtained by summation over pixel data inside the individual subapertures, at a reduced spatial resolution given by the pitch of the segmenting array. As has been demonstrated for visible laser radiation, in case of coherent sources the knowledge of beam profile $I(x, y)$ and wavefront $w(x, y)$ allows for calculation of the relevant beam parameters [5–7]. For this purpose the moments method described in [5, 7, 8] is applied: The central second spatial (x, y) and angular (u, v) moments are computed from the intensity distribution and the local wavefront slopes $\beta_{x,y}$ according to

$$\langle x^2 \rangle = \frac{\sum_{i,j} (x_{ij} - \langle x \rangle)^2 I_{ij}}{\sum_{i,j} I_{ij}} \tag{20.2}$$

$$\langle xu \rangle = \frac{\sum_{i,j} (\beta_{xij} - \langle \beta_x \rangle)(x_{ij} - \langle x \rangle) I_{ij}}{\sum_{i,j} I_{ij}} \tag{20.3}$$

$$\langle u^2 \rangle = \frac{\sum_{i,j} (\beta_{xij} - \langle \beta_x \rangle)^2 I_{ij}}{\sum_{i,j} I_{ij}} + \left(\frac{\lambda}{2\pi} \right)^2 \frac{\sum_{i,j} \left(\frac{(\partial_x I)^2}{I} \right)_{ij}}{4 \sum_{i,j} I_{ij}}, \tag{20.4}$$

where $\langle x \rangle$ and $\langle \beta_x \rangle$ are the first moments over x and β_x [7], respectively; the index (ij) denotes the subaperture. From the second moments the beam width d, divergence θ, beam propagation factor M^2, beam waist diameter d_θ, waist position z_θ and Rayleigh length z_R are computed according to the following equations [7]:

$$d = 4\sqrt{\langle x^2 \rangle}, \qquad \theta = 4\sqrt{\langle u^2 \rangle} \tag{20.5}$$

$$M^2 = \frac{4\pi}{\lambda} \sqrt{\langle x^2 \rangle \langle u^2 \rangle - \langle xu \rangle^2} \qquad d_\theta = \frac{4 M^2 \lambda}{\pi \theta} \tag{20.6}$$

$$z_\theta = \frac{z_R \langle xu \rangle}{|\langle xu \rangle|} \sqrt{\left(\frac{d}{d_\theta} \right)^2 - 1} \qquad z_R = \frac{d_\theta}{\theta}. \tag{20.7}$$

Moreover, once the intensity and the phase distributions are known from a Hartmann measurement, solving Fresnel-Kirchhoff's integral allows numerical propagation of the beam, i.e. computation of intensity distributions at different propagation distances z [9]:

$$I(x, y, z) = \left| \frac{ik}{2\pi z} \iint_{\infty} \sqrt{I(x', y')} e^{ikw(x', y')} e^{\frac{ik[(x-x')^2 + (y-y')^2]}{2z}} \, dx' \, dy' \right|$$

Here x, y and x', y' are the Cartesian coordinates in two coplanar planes separated by z. Thus, in particular the profile at the beam waist position can be predicted, which is in many cases hardly accessable for high power lasers, both due to the high intensity and the small size of the focal spot.

20.2.2 EUV Wavefront Sensor for FEL Characterization

Since currently operating (soft) X-ray FELs are based on the self-amplified spontaneous emission (SASE) process which builds up the laser emission from noise, their beam characteristics can signigicantly differ from pulse to pulse. Therefore, there is a strong requirement for single-pulse photon diagnostics and online characterization of the FEL beam propagation parameters [10, 11]. For this reason a Hartmann wavefront sensor for the extreme UV spectral range was developed and applied for photon diagnostics, beam propagation and optics alignment of the FLASH free electron laser in cooperation with DESY Photon Science/Hamburg [12]. The device was designed to operate from 4 to 40 nm, which is within the accessible FLASH wavelength range. It consists of a pinhole array (Hartmann plate) made of a 20 µm-thick nickel foil with orthogonally arranged electroformed holes (dia. 75 µm, pitch 250 µm) in front of a CCD camera at a distance of 200 mm behind the array (see Fig. 20.2). This distance as well as the dimensions of the Hartmann plate represent a compromise between attainable wavefront sensitivity at short wavelengths and spatial resolution at long wavelengths. For converting the soft X-rays into visible light the CCD chip is coated with a fluorescent coating (Gd_2O_2S:Tb, emission wavelength 545 nm). The Hartmann sensor is adjustable both laterally and with respect to tip and tilt. The device is self-supporting and compact (240 mm × 240 mm × 300 mm) and can be attached behind user experiments.

For absolute at-wavelength calibration of the Hartmann sensor a proper reference wavefront independent of the mentioned pulse-to-pulse fluctuations is essential. For this purpose a spherical wavefront is prepared by spatial filtering, placing a diffracting pinhole (dia. several µm) in the vicinity of the focal spot of the FEL beam. The Hartmann sensor is positioned at a certain distance behind this pinhole, ensuring that its full field of view is illuminated by the central Airy disc. Thereafter, the reference spot distribution is registered (cf. Fig. 20.2, right). A temporally stable spherical wave as described above can also be utilized to assess the sensitivity of the Hartmann sensor.

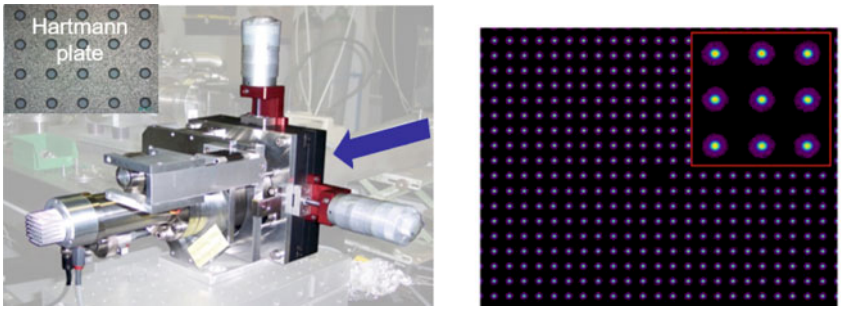

Fig. 20.2 Left: EUV Hartmann sensor with integrated tip/tilt and lateral adjustment; the inset shows a close-up of the Hartmann pinhole plate. Right: spot pattern of the reference wavefront ($\lambda = 13.5$ nm). The central pinhole is omitted for tip/tilt alignment

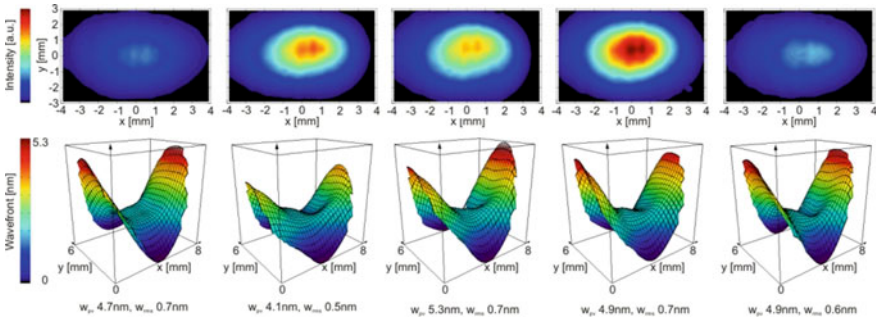

Fig. 20.3 Intensity profiles and wavefronts of single pulses at FLASH BL2 without focusing mirror ($\lambda = 7\,\text{nm}$)

At FLASH beamline BL2 the single pulse wavefront repeatability was determined, recording a series of 100 single FEL pulses behind a 5 µm pinhole at an emission wavelength of 13.8 nm. A root-mean-square deviation $\Delta w_{\text{rms}} = 0.12\,\text{nm}$ ($\lambda/116$) was evaluated, defining an upper limit for the achievable measurement precision of the wavefront sensor.

After these qualification tests the Hartmann sensor was used to analyze the FEL beam of FLASH, at first without focusing mirror [13]. Beam profiles and wavefronts recorded at BL2 for single pulses at a wavelength of 7 nm are displayed in Fig. 20.3, showing relatively strong pulse-to-pulse fluctuations as typical for the SASE process. The saddle-like shape of the wavefront indicates an astigmatism of the beam. Nevertheless, the peak-to-valley (w_{pv}) and root-mean-square (w_{rms}) wavefront aberrations computed after tip/tilt and defocus subtraction of the measured wavefronts are relatively low ($w_{\text{rms}} \sim \lambda/10$).

Neglecting influences from partial coherence (cf. Sect. 20.3), the beam propagational parameters can be computed from the measured intensity and wavefront distributions according to the moments method described above (20.8)–(20.11). Corresponding beam characteristics are compiled in Table 20.1, taking the average over 20 single pulses. Despite the observed astigmatism (waist separation $x - y = 10\,\text{m}$), the evaluated M^2 value of 1.15 is remarkably low, which can be explained by the small higher order wavefront expansion coefficients and the smooth intensity profile.

In contrast to these data, wavefront measurements performed behind beam line optics can lead to much less satisfactory results, caused by an insufficient fine-adjustment of the optics. An example is shown in Fig. 20.4 (left) for an ellipsoidal focusing mirror at BL 3 of FLASH: for this carbon-coated grazing incidence mirror with 2 m focal length the w_{pv} and w_{rms} values of the recorded wavefront are more than an order of magnitude higher than without focusing optics. However, by on-line wavefront diagnostics the EUV Hartmann sensor allows for fine-tuning the mirror alignment. As seen from Fig. 20.4, the dominating strong astigmatism introduced by the optical element could be completely removed by real-time optimizing the pitch and yaw angles of the ellipsoidal mirror. After alignment a w_{pv} of 12 nm and a w_{rms} of 1.1 nm ($<\lambda/10$) could be achieved.

Table 20.1 Beam parameters of FLASH computed from Hartmann data (BL2, $\lambda = 7$ nm)

Beam parameters	X	Y
w_{pv} [nm]	5.3 ± 0.69	
w_{rms} [nm]	0.67 ± 0.09	
Beam propagation parameter M^2	1.15 ± 0.08	
Beam propagation parameter M_i^2	1.23 ± 0.1	1.1 ± 0.1
Beam width d [mm]	6 ± 0.2	4.4 ± 0.1
Waist position $z_{0,i}$ [m]	-109.2 ± 0.9	-99.2 ± 1.4
Rayleigh length z_R [mm]	3760 ± 484	5090 ± 731
Waist diameter $d_{0,i}$ [µm] 2nd moment	200 ± 20	223 ± 25
Divergence θ [µrad]	55 ± 2	44 ± 2

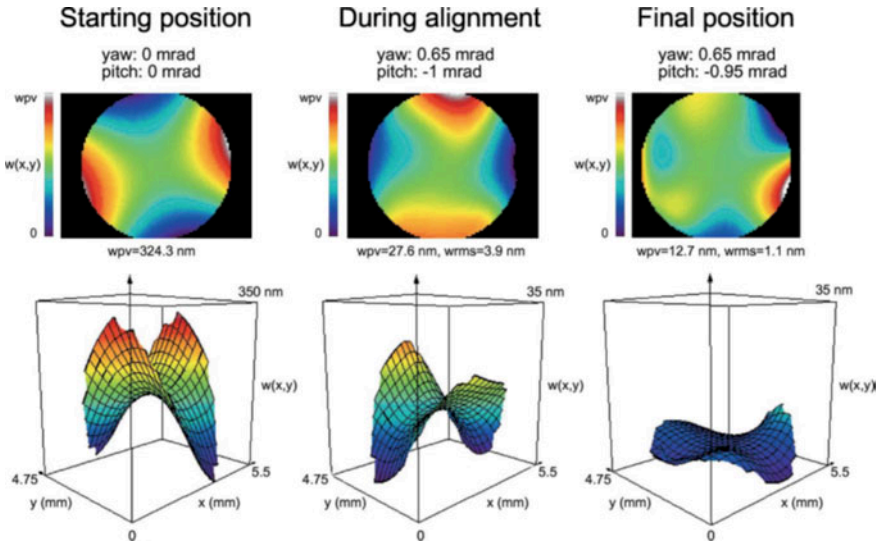

Fig. 20.4 Wavefronts measured at different steps of the alignment procedure of the ellipsoidal focusing mirror at FLASH beamline BL3 ($\lambda = 13.3$ nm). Note that the scale $w(x, y)$ is enlarged by a factor of ten for the starting position to account for the very large initial astigmatism

After optimized fine-adjustment of the focusing element, a Fresnel-Kirchhoff integration of the Hartmann data allows for propagation of the beam, as described in Sect. 20.2.1. Corresponding results recently obtained at FLASH II are displayed in Fig. 20.5 for three z-positions close to the beam waist [14]. The propagated profiles are currently compared with PMMA imprints taken at the respective positions by J. Chalupský et al. (Acad. of Sci., Czech Republic).

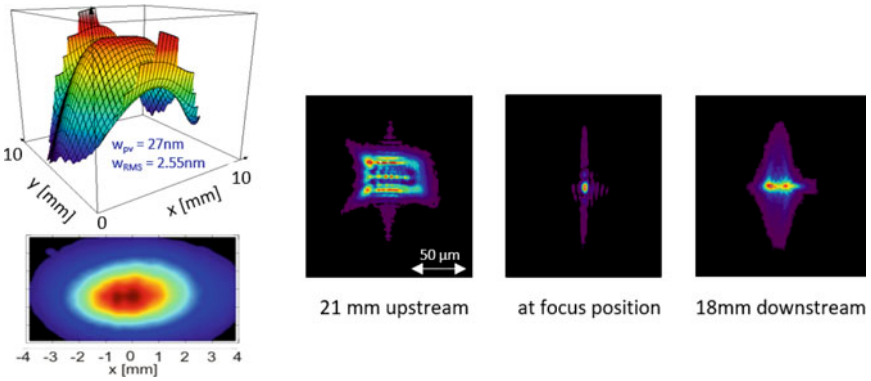

Fig. 20.5 Left: Wavefront and intensity distribution of FLASH 2 (FL24, $\lambda = 13.5$ nm) recorded ~2 m behind KB optics with EUV Hartmann sensor; right: Profiles obtained by Fresnel-Kirchhoff back propagation of the Hartmann data to the beam waist

20.2.3 Beam Characterization of High-Harmonic Sources

The EUV Hartmann wavefront sensor successfully applied for beam characterization at FELs was also employed to investigate EUV radiation generated by High-Harmonic (HHG) sources. Especially for their use in CDI experiments, a proper alignment is crucial since successful reconstruction of phase objects can only be achieved if the phase distortions of the probe beam are negligible. In cooperation with Claus Ropers' group, the propagation of the 25th harmonic ($\lambda = 32$ nm) of a Ti:Saphire laser was studied after passing a toroidal grating that combines spectral filtering and focusing. The Hartmann sensor was positioned behind the focus, capturing the EUV wavefront while the angle of incidence of the harmonic on the grating was varied. As for the FEL beam line mirrors, the recorded wavefront initially shows a strong astigmatism (cf. Fig. 20.6, left), which can be minimized by real-time alignment. A description of the corresponding beam propagation by matrix methods [15] yields good agreement to the experimental data, especially the astigmatic waist difference (cf. Fig. 20.6 right, blue line). From the theoretical computations, the achievable beam intensity is estimated as a function of the incidence angle. As expected, the highest photon flux is obtained for an angle of incidence where the astigmatic aberration disappears. Apparently, already a slight misalignment of 0.5° leads to a decrease of the achievable intensity by 50% compared to its optimum. Thus, in order to achieve short exposure times and prevent reconstruction errors for following CDI experiments, this alignment procedure plays an essential role. With the correspondingly optimized HHG source, it was possible to successfully image test samples at the diffraction limit [16].

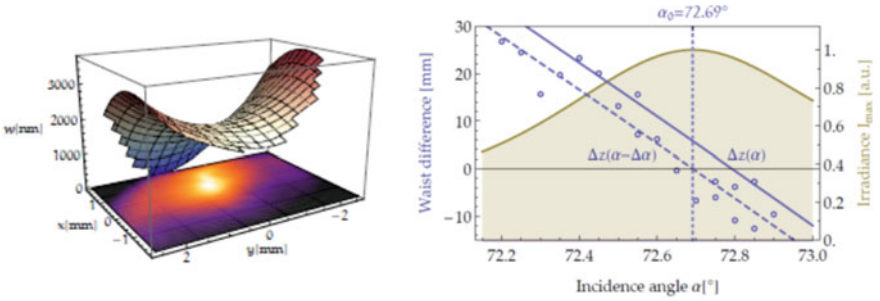

Fig. 20.6 Left: Wavefront (3D) and intensity profile (below) of a HHG beam (25th harmonic). Right: Astigmatic waist difference Δz and achievable irradiance $I_{\max}$ plotted as a function of the angle of incidence on toroidal grating. The theoretical curve $\Delta z(\alpha)$ (solid blue line) lies slightly above the experimental values (blue dots) [15]

20.2.4 Thermal Lensing of X-ray Optics

In addition to static aberrations of optical components given by figure errors or misalignment, beam propagation can also be deteriorated by transient distortions of the wavefront introduced by the beam itself due to local heating and surface deformation (thermal lensing). In order to investigate the influence of this effect on the performance of X-ray optics, in particular high power mirrors to be employed for the European XFEL/Hamburg, we have performed time-resolved wavefront measurements in pump-probe experiments at the ESRF/Grenoble [9]. In this investigation a Si mirror sample was exposed to an intense 15 keV beam, and its thermally induced surface deformation was monitored by measuring the wavefront of a reflected optical laser probe beam with the help of a Hartmann-Shack wavefront sensor (cf. Fig. 20.7). By reconstructing and back propagating the wavefront, the deformed surface could be retrieved for each time step. Thus, the dynamics of the created heat bump, especially its build-up, maximum amplitude and relaxation, were analyzed with a surface

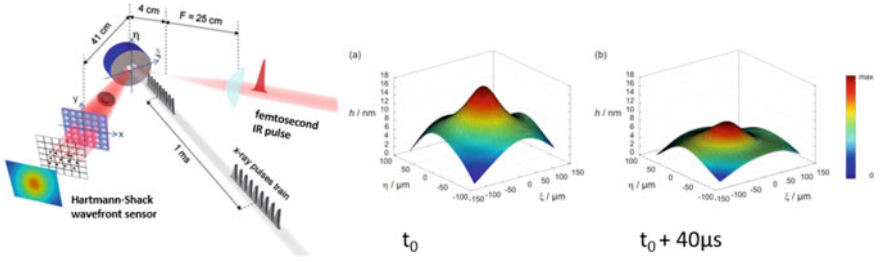

Fig. 20.7 Left: Schematic view of pump-probe setup to determine thermal wavefront distortions of high power X-ray optics at ESRF. Right: surface topology of a Si mirror reconstructed from wavefront measurements for different delays between the X-ray pump and infrared probe pulse. The decay of the heat bump on the mirror proceeds at a time scale of several ten microseconds

height resolution in the nanometer range. For the investigated Si sample deformations induced by a bunch train of X-ray pulses were in the order of several ten nanometers (peak-to-valley); a relaxation time constant of $\sim$30 µs was obtained. The data were interpreted taking into account results of finite element method simulations. Due to its robustness and simplicity this method can find further applications at new X-ray light sources (FEL), or to gain deeper understanding on thermo-dynamical behavior of highly excited materials under non-equilibrium conditions.

20.3 Wigner Distribution for Diagnostics of Spatial Coherence

Apart from the beam profile and shape of the wavefront, the degree of lateral coherence of a beam has a crucial impact on the minimum achievable focal spot size. Whereas both wavefront and irradiance distribution may be discovered from a single shot experiment, the latter is not true for the spatial degree of coherence γ, which is, like the mutual intensity J [17] defined on a four-dimenesional space of lateral position $\mathbf{x}$ and mutual distance $\mathbf{s}$. Earlier approaches for spatial coherence measurement at FELs utilize Young's double pinhole experiment [18] to derive the latter from fringe visibility in the corresponding interference patterns. However, any substantial mapping of $(\mathbf{x}, \mathbf{s})$-pairs requires a vast number of pinhole arrangements and image recordings to be evaluated, which appears to be very inefficient with respect to the experimental effort. Therefore, those measurements have only been carried out for a few selected points $\mathbf{x}$ within the beam profile and one or two perpendicular directions of the pinhole separation vector $\mathbf{s}$. An alternative approach is based on the investigation of lateral correlation of local intensity fluctuations in the beam profile [19]. Although this method is more efficient than Young's experiment, only the modulus of γ can be specified.

In order to determine the full complex degree of coherence, an alternate strategy has been employed to recover the mutual intensity $J(\mathbf{x}, \mathbf{s})$, i.e. through a measurement of the Wigner distribution function (WDF) $h(\mathbf{x}, \mathbf{u})$, representing the two-dimensional Fourier transform of the mutual coherence function [20]. Prior to the presentation of experimental setups and results the theoretical background of the applied formalism will be briefly summarized.

20.3.1 Theory

The Wigner distribution $h(\mathbf{x}, \mathbf{u})$ of a quasi-monochromatic paraxial beam is defined in terms of the mutual intensity $J(\mathbf{x}, \mathbf{s})$ as a two-dimensional Fourier transform of the latter [21]

$$h(\mathbf{x}, \mathbf{u}) = \left(\frac{k}{2\pi}\right)^2 \int J\left(\mathbf{x} - \frac{\mathbf{s}}{2}, \mathbf{x} + \frac{s}{2}\right) e^{ik\mathbf{u}\cdot\mathbf{s}} \, \mathrm{d}s_x \, \mathrm{d}s_y,$$

where $\mathbf{x} = (x, y)$ and $\mathbf{s} = (s_x, s_y)$ denote spatial and $\mathbf{u} = (u, v)$ angular coordinates in a plane perpendicular to the direction of beam propagation, and k is the mean wave number of light. Propagation of the Wigner distribution h and its 4D Fourier transform $\tilde{h}$ through static and lossless paraxial systems from an input (index i) to an output (index o) plane, signified by a 4×4 optical ray propagation $ABCD$ matrix S, writes [22, 23]:

$$h_i(D\mathbf{x} - B\mathbf{u}, -C\mathbf{x}, +A\mathbf{u}) = h_o(\mathbf{x}, \mathbf{u}) \tag{20.8}$$

$$\tilde{h}_i(A^T\mathbf{w} + C^T\mathbf{t}, B^T\mathbf{w} + D^T\mathbf{t}) = \tilde{h}_o(\mathbf{w}, \mathbf{t}), \tag{20.9}$$

where $(\mathbf{w}, \mathbf{t})$ are the Fourier space coordinates corresponding to $(\mathbf{x}, \mathbf{u})$. Considering a set $\{p\}$ of parameters, defined by the optical system being employed to generate projections of the phase space, and a set of irradiance profiles $I_{\{p\}}$ recorded at positions which are connected to an arbitrary reference plane via corresponding ray transformation matrices $S_{\{p\}}$, one obtains:

$$\int h_{\{p\}}(\mathbf{x}, \mathbf{u}) \, \mathrm{d}u \, \mathrm{d}v = I_{\{p\}}(\mathbf{x}) \overset{\mathrm{FT}}{\leftrightarrow} \tilde{h}_{\{p\}}(\mathbf{w}, \mathbf{t} = 0) = \tilde{I}_{\{p\}}(\mathbf{w}) \tag{20.10}$$

and from (20.9) and (20.10) [24]:

$$\tilde{h}_{\mathrm{ref}}(A^T_{\{p\}}\mathbf{w}, B^T_{\{p\}}\mathbf{w}) = \tilde{I}_{\{p\}}(\mathbf{w}). \tag{20.11}$$

Propagation through free space in beam direction (z axis) is described by the $ABCD$ matrix

$$S_z = \begin{pmatrix} 1 & z \\ 0 & 1 \end{pmatrix} \tag{20.12}$$

corresponding to the detector position in the experimental arrangement described below. Thus, (20.10) becomes

$$\tilde{h}_{\mathrm{ref}}(\mathbf{w}, z \cdot \mathbf{w}) = \tilde{I}_z(\mathbf{w}), \tag{20.13}$$

representing a four-dimensional mapping relation between Fourier transformed intensity distributions and the Wigner distribution of the beam (Projection Slice Theorem). Following this equation, the phase space of $\tilde{h}$ is filled with data from intensity profiles measured at several z-positions, as for instance obtained from a caustic scan of the beam. A subsequent four-dimensional inverse Fourier transform of $\tilde{h}$ results in the Wigner distribution function.

The global degree of coherence K is calculated by

$$K = \frac{\lambda^2}{P^2} \int h(\mathbf{x}, \mathbf{u})^2 \, \mathrm{d}x \, \mathrm{d}y \, \mathrm{d}u \, \mathrm{d}v, \tag{20.14}$$

(P = total power of the beam) and the mutual coherence function is derived by a two-dimensional Fourier back-transform

$$J(\mathbf{x}, \mathbf{s}) = \int h(\mathbf{x}, \mathbf{u}) e^{-ik\mathbf{u}\cdot\mathbf{s}} \, \mathrm{d}u \, \mathrm{d}v. \tag{20.15}$$

The coherence lengths l_x and l_y are deduced as half width at half maximum of $J(0, 0, s_x, 0)$ and $J(0, 0, 0, s_y)$, respectively.

20.3.2 Experimental Results

As mentioned above, the Wigner distribution can be derived from intensity profiles along the propagation direction of a beam. Figure 20.8 shows the corresponding experimental setup employed for caustic measurements of the FEL FLASH. Here, focusing is achieved by a carbon-coated ellipsoidal mirror with a focal length of 2 m. The EUV sensor consists of a phosphorous screen imaged onto a CCD chip by a 10x magnifying microscope. A motorized translation stage allows for movement of the detector in z-direction within a range of 250 mm, covering up to ten Rayleigh lengths z_R in both directions around the beam waist. During the caustic measurement, FLASH was running in single bunch mode at a wavelength of $\lambda = 25$ nm. Typically, profiles are acquired at more than 100 different z-positions around the beam waist.

FEL beam profiles at three positions in the focal region behind the ellipsoidal mirror are displayed in Fig. 20.8, indicating pronounced vertical stripes which can be attributed to a residual ripple-like corrugation of the mirror surface [25], while for

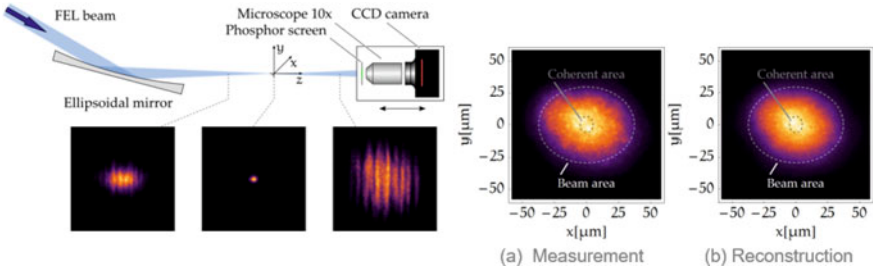

Fig. 20.8 Left: Experimental setup for the Wigner distribution measurement at FLASH and selected profiles close to the beam waist at $\lambda = 25$ nm. Right: Measurement of the beam profile at mean waist position together with reconstruction from the obtained Wigner distribution. Ellipses indicate the coherent fraction of the beam area

Table 20.2 Beam propagation parameters of FLASH evaluated from Wigner measurements (beam waist diameter d_0, Rayleigh length z_R, beam quality factor M^2, coherence length l and global degree of coherence K)

	d_0 [µm]	z_R [mm]	M^2	l [µm]	K
x-direction	67	12.2	8.6	9.0	0.032
y-direction	53	4.3	4.6	11.6	0.032

y-direction the profiles are distributed much smoother. In the focal position the structure vanishes into a uniform distribution. From the Wigner distribution function computed according to the previous section we reconstruct beam profiles at arbitrary positions z in the following fashion: $h(\mathbf{x}, \mathbf{u})$ is propagated via (20.8) applying propagation matrix $S_{\{p\}}$ from (20.12), subsequently the near field of the beam is generated by the integration $I_z(\mathbf{x}) = \int h_z(\mathbf{x}, \mathbf{u})\, \mathrm{d}u\, \mathrm{d}v$. The resulting reconstructed intensity distribution at average waist position is displayed in Fig. 20.8 (right) together with the corresponding experimental profile. Apparently, a good agreement between measured and reconstructed intensity distribution is achieved which confirms the validity of the obtained Wigner distribution. From the mutual coherence function J of the beam, reconstructed at the average waist position by application of (20.15), the coherence lengths l_x in horizontal and l_y in vertical direction can be calculated as HWHM values of the 1D slices $J(0, 0, s_x, 0)$ and $J(0, 0, 0, s_y)$. The dotted curves in Fig. 20.8 show the corresponding ellipses $s_x^2/l_x^2 + s_y^2/l_y^2 = 1$ and $x^2/d_x^2 + y^2/d_y^2 = 1$, indicating the coherence area and total beam area, respectively. It is appearent, that the coherence length corresponds to a small fraction of the beam diameter only. The exact values are given in Fig. 20.2. The coherence for the vertical beam direction is found to be significantly larger than for horizontal direction. Furthermore, the global degree of coherence is calculated as $K = 0.032$, unveiling an apparently low coherence of the FLASH beam.

In comparison with existing coherence measurements based on Young's double slit good agreement is found for the coherence lengths, but the global degree of coherence is lower by one order of magnitude. This discrepancy can, at least partly, be explained by the fact that an ensemble of beam profiles is employed for the Wigner evaluation, resulting in beam properties in terms of mean values. In contrast, in Young's experiment individual pulses are analyzed which yield corresponding maximum values [18]. Another issue leading to underestimated values of the global coherence is the incomplete 3D mapping using only profiles from a standard caustic measurement (cf. next section).

20.3.3 4D Wigner Measurements

The described reconstruction of the Wigner distribution based on beam profiles acquired from free space propagation according to (20.13) covers only a 3D sub-

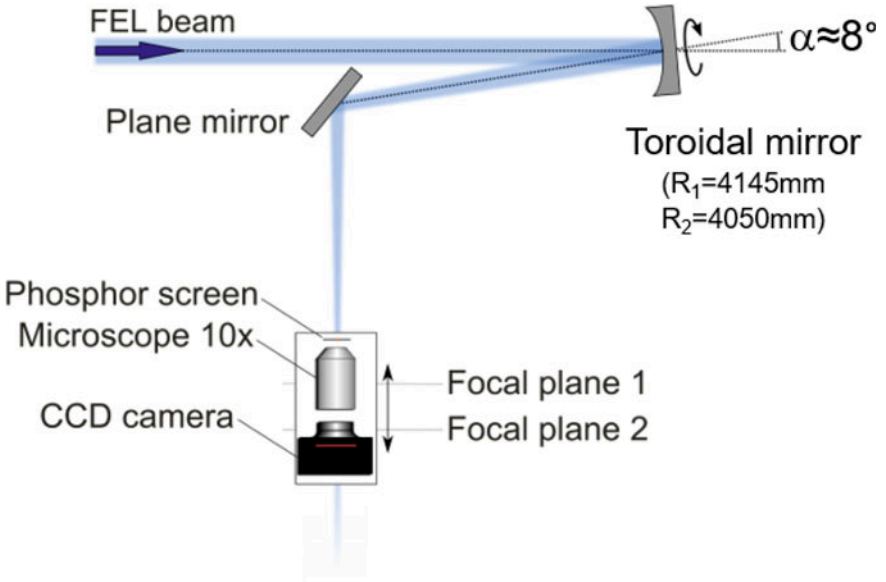

Fig. 20.9 Setup for a 4D measurement of the Wigner distribution

set of the phase space, as z is the only free parameter in the ray propagation matrix (20.12). Although such a reduced mapping is sufficient for some special cases covering e.g. separable or quasi-homogeneous beams and coherent beams with zero twist, the validity of these conditions is not a priori known. Therefore, an extended approach has been established, using, in addition to the detector z-position, the orientation angle ϕ of an astigmatic optical element as mapping parameter. The corresponding ray matrices $S_{\{z,\phi\}}$ [24, 26] permit, according to (20.11), a complete 4D map of the phase space. The extended setup including a non-rotational symmetric element is shown in Fig. 20.9. It applies a rotatable toroidal mirror, introducing a fourth degree of freedom into the system. Thus, choosing measurement parameters (rotation angles, camera positions) properly, it is possible to reconstruct the entire 4D Wigner distribution, also for non-separable beams.

In order to test and qualify the 4D approach, a diode-pumped Nd:YVO_4 laser operating at its fundamental wavelength $\lambda = 1064$ nm (continuous wave) was employed which accomplishes the selective excitation of Hermite-Gaussian modes by pumping the laser crystal at different lateral positions ("mode generator"). TEM_{00}, TEM_{10}, TEM_{02}, TEM_{03} and an uncorrelated superposition of TEM_{10} and TEM_{01} were investigated in a setup similar to Fig. 20.9, using a polished aluminum toroidal mirror (radii 200 and 300 mm) and a standard CCD camera as detector. Rotation of the mirror and movement of the camera has been achieved by servo motors. The automated measurement for each laser mode consists of 410 beam profiles in total, corresponding to 10 rotation angles and 41 z-positions. In Fig. 20.10 the Wigner distribution functions reconstructed from the described measurement are depicted for the TEM_{02}

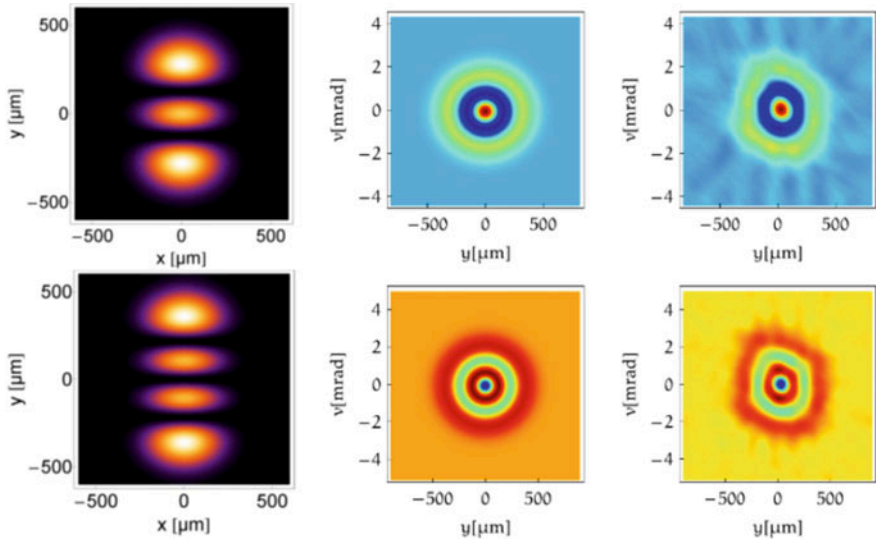

Fig. 20.10 Qualification of 4D Wigner formalism using near IR mode generator for different Hermite-Gaussian beams: Wigner distributions of TEM_{02} and TEM_{03} modes resulting from theory and experiment are shown for comparison

Table 20.3 Global degree of coherence K for different Hermite–Gaussian beams in theory and experiment

	TEM_{00}	TEM_{10}	TEM_{02}	TEM_{03}	$TEM_{10} + TEM_{01}$
Theory	1	1	1	1	0.5
Experiment	0.95	1.06	0.98	0.90	0.46

and TEM_{03} modes, together with the expected theoretical WDFs of the analyzed beams. Obviously, the experimental results correspond nicely to the theory. Also quantitatively, the expected global degree of coherence $K = 1$ is reproduced with an accuracy better than 10 %. As seen from Fig. 20.3, this holds also for the other investigated modes.

After successful qualification, the 4D Wigner method was adapted to the extreme UV wavelength of 13.5 nm by employing a toroidal MoSi multilayer mirror (curvature radii 4145 and 4050 mm, cf. Fig. 20.9), serving to further characterize FEL beams. Recently, first 4D measurements of the WDF have been performed at beamline FL24 of FLASH 2. The data were acquired for the unfocused beam, employing a tilt angle of 8° on the toroid. In total 500 profiles at 50 z-positions and 10 rotation angles were recorded within the 250 mm range of a motorized linear stage. Furthermore, various apertures placed upstream the Wigner setup were utilized in order to modify beam size and spatial coherence properties. The 4D Wigner reconstruction yielded preliminary evaluation results for the global degree of coherence K between

$K = 0.1$ for a 5 mm aperture and $K = 0.25$ for a 3 mm aperture, which is one order of magnitude higher than with the 3D approach. For better comparison to Young's measurements the square root of K is more appropriate, leading to $\sqrt{K} = 0.3$ for the 5 mm and $\sqrt{K} = 0.5$ for the 3 mm aperture diameter, respectively. These values agree qualitatively quite well to results obtained from interference fringe contrast in Young's double pinhole experiments. The observed higher degree of coherence can at least in part be attributed to the focusing optics at FLASH II (high quality Kirkpatrick-Baez mirror instead of slightly corrugated ellipsoidal mirror at FLASH I). Further clarifying work is in progress.

20.4 Conclusion and Outlook

The feasibility of a compact Hartmann wavefront sensor to be employed for beam characterization of FELs and HHG sources emitting in the EUV spectral region has been demonstrated. The device accomplishes simultaneous recording of both wavefront and intensity distributions, allowing for an optimization of the beam transport by fine-tuning the focusing optics. For both FELs and HHG sources we demonstrated that Hartmann wavefront sensor assisted alignment can considerably reduce the astigmatic focal difference induced by grazing incidence mirrors and gratings. The resulting decrease of wavefront error leads to higher spot brightness resulting in an enhanced CDI performance. In case of the FEL FLASH a reduction of residual wavefront aberrations to $w_{\mathrm{rms}} \sim \lambda/10$ could be achieved. Wavefronts and intensity profiles of single FLASH pulses were recorded, accomplishing an analysis of beam fluctuations of the SASE FEL. From these data characteristic propagational parameters of the FLASH beam were computed by applying the moments method. Fresnel-Kirchhoff integration allowed for numerical beam propagation, in particular for an analysis of profiles in the waist region which is hardly accessable for a direct measurement. Future activities will involve extension of the Hartmann approach to harder X-rays in cooperation with European XFEL/Hamburg, as well as an improved prediction of the propagation characteristics by employing a sensor with higher dynamics and spatial resolution.

In addition, it has been shown that the propagation of partially coherent radiation is successfully described by the formalism of the Wigner distribution function. In comparison to existing studies, this is achieved without the need of simplifying assumptions on the beam. It is expected that the obtained comprehensive beam characterization leads to further improvements in the field of CDI and related techniques. Inclusion of coherence information into the propagation formalism will enable a successful prediction of focal intensity distributions and spot sizes even for sources with relatively poor coherence properties.

Acknowledgements The authors like to thank Barbara Keitel and Elke Plönjes (DESY Photon Science) for their support during the measurements at FLASH as well as for stimulating discussions.

References

1. Iso 15367: Lasers and laser-related equipment—test methods for determination of the shape of a laser beam wavefront (2003)
2. Cubalchini, R.: Modal wave-front estimation from phase derivative measurements. JOSA **69**(7), 972–977 (1979)
3. Noll, R.J.: Phase estimates from slope-type wave-front sensors. JOSA **68**(1), 139–140 (1978)
4. Mercère, P., Zeitoun, P., Idir, M., Le Pape, S., Douillet, D., Levecq, X., Dovillaire, G., Bucourt, S., Goldberg, K.A., Naulleau, P.P., et al.: Hartmann wave-front measurement at 13.4 nm with λ euv/120 accuracy. Opt. Lett. **28**(17), 1534–1536 (2003)
5. Schäfer, B., Lübbecke, M., Mann, K.: Hartmann-shack wave front measurements for real time determination of laser beam propagation parameters. Rev. Sci. Instrum. **77**(5), 053,103 (2006)
6. Neal, D.R., Alford, W.J., Gruetzner, J.K., Warren, M.E.: Amplitude and phase beam characterization using a two-dimensional wavefront sensor. In: Third International Workshop on Laser Beam and Optics Characterization, vol. 2870, pp. 72–83. International Society for Optics and Photonics (1996)
7. Schäfer, B., Mann, K.: Determination of beam parameters and coherence properties of laser radiation by use of an extended hartmann-shack wave-front sensor. Appl. opt. **41**(15), 2809–2817 (2002)
8. Iso 11146: Lasers and laser-related equipment—test methods for laser beam parameters—beam widths, divergence angle and beam propagation factor (1999)
9. Gaudin, J., Keitel, B., Jurgilaitis, A., Nüske, R., Guérin, L., Larsson, J., Mann, K., Schäfer, B., Tiedtke, K., Trapp, A., et al.: Time-resolved investigation of nanometer scale deformations induced by a high flux x-ray beam. Opt. Express **19**(16), 15516–15524 (2011)
10. Kuhlmann, M., Plönjes, E., Tiedtke, K., Toleikis, S., Zeitoun, P., Gautier, J., Lefrou, T., Douillet, D., Mercère, P., Dovillaire, S.B.G., et al.: Wave-front observations at flash. Proc. FEL **2006**, (2006)
11. Tiedtke, K., Azima, A., Von Bargen, N., Bittner, L., Bonfigt, S., Düsterer, S., Faatz, B., Frühling, U., Gensch, M., Gerth, C., et al.: The soft x-ray free-electron laser flash at desy: beamlines, diagnostics and end-stations. New J. Phys. **11**(2), 023,029 (2009)
12. Flöter, B., Juranić, P., Kapitzki, S., Keitel, B., Mann, K., Plönjes, E., Schäfer, B., Tiedtke, K.: Euv hartmann sensor for wavefront measurements at the free-electron laser in hamburg. New J. Phys. **12**(8), 083,015 (2010)
13. Flöter, B., Juranić, P., Großmann, P., Kapitzki, S., Keitel, B., Mann, K., Plönjes, E., Schäfer, B., Tiedtke, K.: Beam parameters of flash beamline bl1 from hartmann wavefront measurements. Nucl. Instrum. Methods Phys. Res. Sect. A: Accel. Spectrom. Detect. Assoc. Equip. **635**(1), S108–S112 (2011)
14. Ruiz-Lopez, M.: Wavefront propagation simulations supporting the design of a time-delay compensating monochromator beamline at flash2 (2018). PhotonDiag 2018
15. Mey, T., Zayko, S., Ropers, C., Schäfer, B., Mann, K.: Toroidal grating astigmatism of high-harmonics characterized by euv hartmann sensor. Opt. Express **23**(12), 15310–15315 (2015)
16. Zayko, S., Mönnich, E., Sivis, M., Mai, D.D., Salditt, T., Schäfer, S., Ropers, C.: Coherent diffractive imaging beyond the projection approximation: waveguiding at extreme ultraviolet wavelengths. Opt. Express **23**(15), 19911–19921 (2015)
17. Born, M., Wolf, E.: Principles of Optics: Electromagnetic Theory of Propagation, Interference and Diffraction of Light. Cambridge University Press (2000)
18. Singer, A., Vartanyants, I., Kuhlmann, M., Duesterer, S., Treusch, R., Feldhaus, J.: Transverse-coherence properties of the free-electron-laser flash at desy. Phys. Rev. Lett. **101**(25), 254,801 (2008)
19. Singer, A., Lorenz, U., Sorgenfrei, F., Gerasimova, N., Gulden, J., Yefanov, O., Kurta, R., Shabalin, A., Dronyak, R., Treusch, R., et al.: Hanbury brown–twiss interferometry at a free-electron laser. Phys. Rev. Lett. **111**(3), 034,802 (2013)
20. Bastiaans, M.J.: The wigner distribution function of partially coherent light. Opt. Acta: Int. J. Opt. **28**(9), 1215–1224 (1981)

21. Bastiaans, M.J.: Application of the wigner distribution function to partially coherent light. JOSA A **3**(8), 1227–1238 (1986)
22. Eppich, B., Mann, G., Weber, H.: Measurement of the four-dimensional wigner distribution of paraxial light sources. In: Optical Design and Engineering II, vol. 5962, p. 59622D. International Society for Optics and Photonics (2005)
23. Tran, C., Williams, G., Roberts, A., Flewett, S., Peele, A., Paterson, D., de Jonge, M., Nugent, K.: Experimental measurement of the four-dimensional coherence function for an undulator x-ray source. Phys. Rev. Lett. **98**(22), 224,801 (2007)
24. Schäfer, B., Mann, K.: Characterization of an arf excimer laser beam from measurements of the wigner distribution function. New J. Phys. **13**(4), 043,013 (2011)
25. Mey, T., Schäfer, B., Mann, K., Keitel, B., Kuhlmann, M., Plönjes, E.: Wigner distribution measurements of the spatial coherence properties of the free-electron laser flash. Opt. Express **22**(13), 16571–16584 (2014)
26. Mey, T., Schäfer, B., Mann, K.: Measurement of the wigner distribution function of non-separable laser beams employing a toroidal mirror. New J. Phys. **16**(12), 123,042 (2014)